Base wake dynamics and its influence on driving stability of passenger vehicles in crosswind

(article starts on next page)

Base wake dynamics and its influence on driving stability of passenger vehicles in crosswind

Adam Brandt [a,b,*], Simone Sebben [a], Bengt Jacobson [a]

[a] Department of Mechanics and Maritime Sciences, Chalmers University of Technology, Gothenburg 41296, Sweden
[b] CEVT (China Euro Vehicle Technology), Gothenburg 41755, Sweden

ARTICLE INFO

ABSTRACT

The unsteady flow around a travelling vehicle induces fluctuating aerodynamic loads. Automotive manufacturers usually set targets on the time-averaged lift forces to ensure good straight-line stability performance at high speeds. These targets are generally sufficient in preventing unstable vehicle designs. Yet, small changes in averaged values occasionally yield unexpectedly large differences in the stability performance, indicating that the changes in averaged normal loads cannot solely explain these differences. The unsteady aerodynamic effects on driving stability are, therefore, an interesting topic to study. The objective of the present work is to investigate the differences in wake dynamics and fluctuating aerodynamic loads for two variants of a roof spoiler on a sports utility vehicle: a baseline that was known to cause stability issues and an improved design which resolved them. The vehicle designs were investigated using accurate time-resolved CFD simulations for a set of crosswind conditions. The unsteady aerodynamic response was coupled to a vehicle dynamics model to analyse the resulting impact on driving stability. It was shown that in crosswinds the baseline spoiler, contrary to the improved spoiler, has bi-stable wake dynamics that induce lift force fluctuations at frequencies close to the 1st natural frequency of the rear suspension.

1. Introduction

Customers expect a high level of perceived control and stability in modern passenger vehicles. The automotive industry needs to fulfil this while still striving towards high-efficiency vehicles with low aerodynamic drag. This requires interdisciplinary understanding of coupled aerodynamic and vehicle dynamic driving stability. While aerodynamic loads increase quadratically with vehicle speed, the vehicle dynamic yaw damping is reduced making vehicles more sensitive at high speeds. The correlation between the straight-line driving stability performance and the aerodynamic lift forces is well-known in the automotive industry (Schuetz, 2015). When developing new passenger vehicles, the time-averaged aerodynamic lift coefficients are often used for target setting. The aerodynamic lift forces influence the tyre normal loads which affect the cornering stiffness and thus the vehicle dynamic handling. Buchheim et al. (1985) used the static stability index, introduced by Milliken et al. (1976), to show that a positive front-to-rear lift balance $(C_{lf} - C_{lr})$ increases the stability of the vehicle. This was later confirmed in studies by Windsor and Le Good (1993) and Howell and Le Good (1999). The subjective high speed stability ratings from on-road experiments correlated well with the aerodynamic lift balance of the vehicles, where higher front-to-rear lift balance correlated with

better stability ratings (Howell and Le Good, 1999). This knowledge has since been used by the automotive industry to indicate potential stability problems during development and requirements are usually set on the aerodynamic lift forces at each axle and the balance between the two. Nevertheless, there are experiences where small changes in time-averaged lift forces have an effect on the stability performance which is more significant than what can be solely explained by the change in normal loads. This indicates that important information is lost when averaging the forces.

More recently, Okada et al. (2009) showed correlation between the transient aerodynamic flow structures and the on-road subjective assessment of a vehicle. Kawakami et al. (2015) correlated the subjective assessment to the roll and yaw moment fluctuations and showed that the fluctuations could be reduced by using a roof-side spoiler design and delta-winglet vortex generators mounted on the sides at the rear of the vehicle. The vortex generators were evaluated subjectively on a test vehicle, where improvements in driving stability were noted. A similar numerical study used a methodology based on DMD (dynamic mode decomposition) to find geometrical improvements for reducing the pitching moment fluctuations at 1.2 Hz (Matsumoto et al., 2019), a problematic frequency since it lies close to the pitching mode of the

---

* Corresponding author at: Department of Mechanics and Maritime Sciences, Chalmers University of Technology, Gothenburg 41296, Sweden.
E-mail address: adam.brandt@chalmers.se (A. Brandt).

(a) Test object.

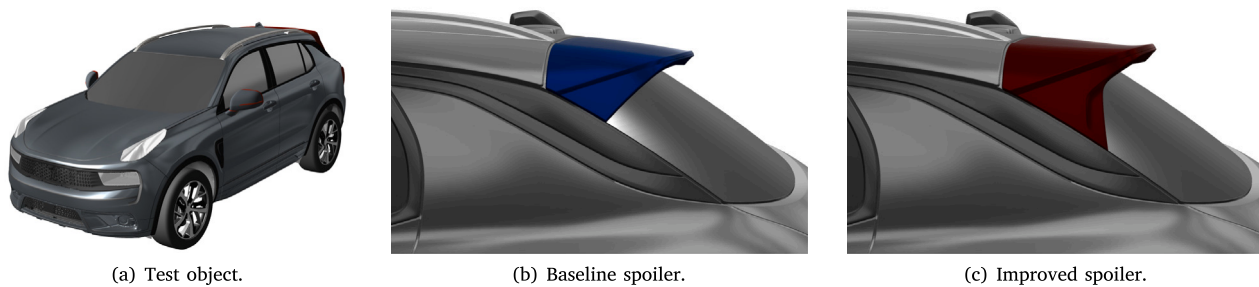(b) Baseline spoiler.

(c) Improved spoiler.

Fig. 1. Rendered images of the vehicle, the baseline spoiler (blue) and the improved spoiler (red), used in this study. (For interpretation of the references to colour in this figure legend, the reader is referred to the web version of this article.)

suspension system in a typical passenger vehicle ($\approx 1.0 - 1.5$ Hz). The fluctuations were successfully reduced by adding new design solutions at the rear-side spoiler, under the vehicle and at the front wheels. These studies indicate that the aerodynamic load fluctuations influence the vehicles' stability performance and that clever design solutions can reduce these fluctuations.

In Brandt et al. (2020), the authors reported that the frequency of events with poor stability performance increased when driving in crosswind conditions. Hence, optimising the aerodynamic design for ideal conditions without crosswind can lead to poor stability performance when the vehicle is subjected to yawed flow conditions. On-road measurements have shown that the relative flow angle typically varies between ± 10 deg for a vehicle travelling on the highway (Wojciak, 2012; Theissen, 2012; Lawson et al., 2008; Jessing et al., 2020). Furthermore, the turbulence intensity (TI) is generally much higher on the road, with typical values of 2% to 10% compared to <1% in conventional wind tunnels (Wordley and Saunders, 2008, 2009; Lawson et al., 2008; Cooper and Watkins, 2007). Optimising the design of a vehicle for low drag in these two different turbulence intensity flows has been shown to yield different optimum designs of the backlight angle (Watkins and Cooper, 2007). Thus, a broader range of flow conditions should be considered during aerodynamic development to ensure robust aerodynamic vehicle designs.

The aerodynamic load fluctuations on a bluff body, such as a passenger vehicle, are to a large extent determined by the dynamics of the wake aft the body. Large unsteady wake motions will result in significant load fluctuations. Furthermore, the shape of the wake can indicate some aerodynamic characteristics of the vehicle, such as a higher rear lift for a down-wash dominated wake versus an up-wash dominated wake. Urquhart et al. (2020) found that optimising the roof and side angles for low drag on a simplified vehicle geometry (Windsor model) resulted in a vertically balanced wake that is neither up-wash nor down-wash dominated. Interestingly, simplified geometries, such as the Windsor and Ahmed body, with presumably balanced wakes have shown to have bi-stable wake dynamics, where the wake randomly switches between two asymmetrical but mirrored states (Grandemange et al., 2013, 2015). The aspect ratio of the base determines the orientation of the bi-stability, where the wake state switches from left to right for a broad base and top to bottom for a tall base (Grandemange et al., 2013), also referred to as symmetry breaking modes (Bonnavion et al., 2019). Nonetheless, these effects were quite sensitive since they disappeared when subjecting the models to slight crosswind flows (Perry et al., 2016; He et al., 2022). However, Meile et al. (2016) showed that vertical wake bi-stability could occur in crosswind conditions when adding a slanted rear windscreen angle of 35 deg to the Ahmed body. For this geometry, the bi-stability only occurred at certain crosswind conditions (Meile et al., 2016). This led to the reasoning that real passenger vehicles with slanted rear windscreen angles could exhibit wake bi-stabilities in crosswinds, which was confirmed in a study by Bonnavion et al. (2017) investigating a hatchback vehicle. Similarly,

this vehicle geometry only exhibited the vertical switching between wake states in a specific range of the relative flow angle. The wake data difference between the states was not as evident as for the simplified bodies, yet two statistically preferred vertical base pressure gradient states were found. The two states were predominantly determined by either an attached or detached flow over the rear windscreen in these crosswind conditions (Bonnavion et al., 2017). Vertical wake multi-stabilities have also been found in studies on light vans (Cadot et al., 2016; Bonnavion et al., 2017, 2019).

The above suggests that only targeting the time-averaged aerodynamic lift coefficient might not be enough to guarantee good straight-line driving stability at high speeds. Therefore, understanding the influence of unsteady aerodynamic loads on driving stability is essential in developing low-drag and stable passenger vehicles. This paper investigates two design variants of the rear roof spoiler on a real sports utility vehicle (SUV). Both spoilers have time-averaged lift coefficients within the set requirements. Yet, the baseline spoiler (which was the first suggested design) showed lower straight-line stability performance at high speeds and has been used in a previous on-road study by the authors (Brandt et al., 2020), while the improved spoiler, used in the production version of the vehicle, solved all the high speed stability issues. This study analyses how the wake dynamics differ between spoilers, for multiple angles of the incoming flow, and investigates how this influence the aerodynamic fluctuations, and consequently, the vehicle dynamic handling and the driver's perceived level of control and stability.

2. Methodology

This section presents the vehicle geometry and the two roof spoiler designs. The numerical simulation procedure, the mesh sensitivity analysis and the data post-processing are then described, followed by the coupling between aerodynamics and vehicle dynamics.

2.1. Geometry

This study used a fully-detailed compact sports utility vehicle (SUV). The test object is 4.51 m in length, 1.60 m in height, 1.86 m in width, has a wheel base of 2.73 m and a track width of 1.60 m. The vehicle mass is 1845 kg, with 57% of the static load on the front axle. The suspension system consisted of a MacPherson front suspension and a 4-link trailing arm rear suspension. Coil springs and passive dampers control the system. The virtual model includes a detailed underbody and engine bay, with 235/50 R19 tyres modelled as slicks. The model and its two versions of the spoiler can be seen in Fig. 1. Compared to the baseline, the improved spoiler has a more aggressive kick and it features larger corner fillers between the spoiler and the D-pillar.
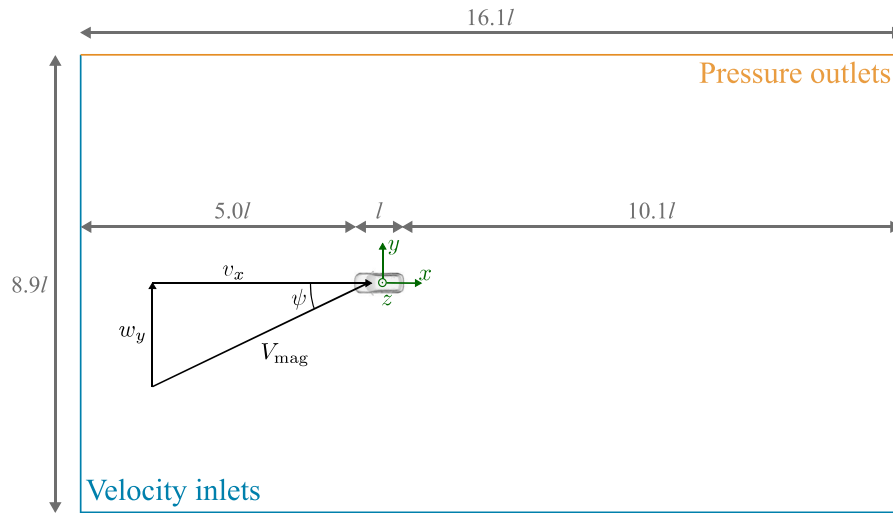
Fig. 2. Top view of the computational domain with the inlet and outlet boundaries marked in blue and orange, respectively. The coordinate system and the relations between the flow angle, ψ, flow velocity, V_{mag}, vehicle velocity, v_x, and lateral wind component, w_y, are also shown. (For interpretation of the references to colour in this figure legend, the reader is referred to the web version of this article.)

Table 1
Solver settings.

Turbulence model	SBES SST k-ω
Sub-grid scale model	Dynamic Smagorinsky model (DSM)
Pressure–velocity coupling	Coupled
Gradient scheme	Least Squares cell-based
Pressure discretisation	Second-order
Momentum discretisation	Bounded Central Difference
Turbulence discretisation	Second-order
Temporal discretisation	Bounded second-order implicit
Time step size	1.6×10^{-4} s
Inner iterations	4

2.2. Numerical setup

A constant vehicle velocity, v_x, of 160 km/h was used. Fig. 2 visualise the flow components, where the crosswind velocities, w_y, were chosen to match the investigated flow angles, ψ, of 0, 1.25, 2.5, 5 and 7.5 deg. These flow components (v_x and w_y) formed the boundary conditions at the velocity inlets. Zero-pressure boundary conditions was used at the outlets, opposite to the inlets. The roof had a zero-gradient boundary condition while the ground was modelled as a moving wall with the longitudinal velocity, v_x. The tyres had moving (rotating) wall conditions while the rim rotations were modelled using moving reference frames (MRFs). The domain size was sufficiently large to avoid any effects from the inlet and outlet and had a blockage of less than 0.4%. The length of the domain was $16.1l$, the width $8.9l$ and the height $4.4l$, where l is the vehicle length.

Scale-resolving simulations (SRS) using the stress-blended eddy simulation (SBES) turbulence model (Menter, 2018) with the SST k-ω in the RANS region and the dynamic Smagorinsky model (DSM) (Germano et al., 1991) for the sub-grid scale modelling in the LES region were performed with the commercial cell-centred finite volume solver ANSYS Fluent (version 2021R2). The choice of the DSM was based on the conclusions of Ekman et al. (2021), where the DSM showed excellent agreement with experimental data for predicting flow separation on the Ahmed body. All dependent variables were discretised using second-order accurate discretisation schemes. For the velocity components, the bounded central difference scheme was used, while the turbulence quantities were discretised using the second order upwind scheme. The bounded second-order implicit temporal scheme was used to advance in time. All solver settings are summarised in Table 1.

The unsteady simulations were initialised with steady-state RANS, followed by a 2 s unsteady solution for flushing the domain and setting the final solver settings. Then, the simulations were run for 5 s physical time to resolve any low-frequency fluctuations at 0.5–2 Hz (St = 0.05 − 0.2). The time-averaged data presented in this work was averaged during these 5 s, corresponding to 49 convective flow units ($t \cdot v_{mag}/l$), where t is the physical time and v_{mag} the free-stream velocity.

2.3. Mesh, time step study and experimental validation

The mesh count and the size of the time step were investigated in a study performed at 160 km/h in 5 deg yawed flow. The results of this study were evaluated against available wind tunnel data to confirm the accuracy of the simulation setup and justify the selection of a methodology with reasonable computational cost.

2.3.1. Mesh size

Four volume meshes were created with different levels of refinement, resulting in the four total cell counts seen in Table 2. The first cell heights at the walls were kept equal for all meshes, resulting in a $y^+ \approx 1$ for the exterior, wheels and the underbody panels, as recommended for the turbulence model used Menter (2018). The results in Table 2 show the deltas between a wind tunnel test of the vehicle and the time-averaged results from the simulations. It is evident that there are some differences between wind tunnel and CFD regardless of mesh size, especially for the lift coefficients (C_{lf} and C_{lr}). These differences are likely caused by the moving ground and blockage effects in the wind tunnel at yawed flow versus the open-road scenario simulated in CFD (Wickern and Beese, 2002; Ljungskog, 2019; Josefsson, 2022). All meshes perform equally well in predicting the drag force coefficient (C_D) and although the lift forces were under-predicted, the balance between the front and rear lift ($C_{lf} - C_{lr}$) was close to the experimental data for the two finest mesh sizes. Since the balance between front and rear lift has a large impact on driving stability (Howell and Le Good, 1999), the coarse and medium mesh sizes were considered unsuitable and the fine mesh was selected for this study since it showed similar accuracy as the extra fine mesh but with significantly lower computational cost. The fine mesh had 15 prism layers on the exterior. Fig. 3 includes a zoomed view of the prism layers, where a gradual growth between the prism layers, the intermediate tetrahedral layer and the hexahedral mesh can be observed. The top view in Fig. 3 shows three of the refinement zones' sizes, while cell sizes as small as 4.25 mm were used around the wheels, the spoiler and curved surfaces.
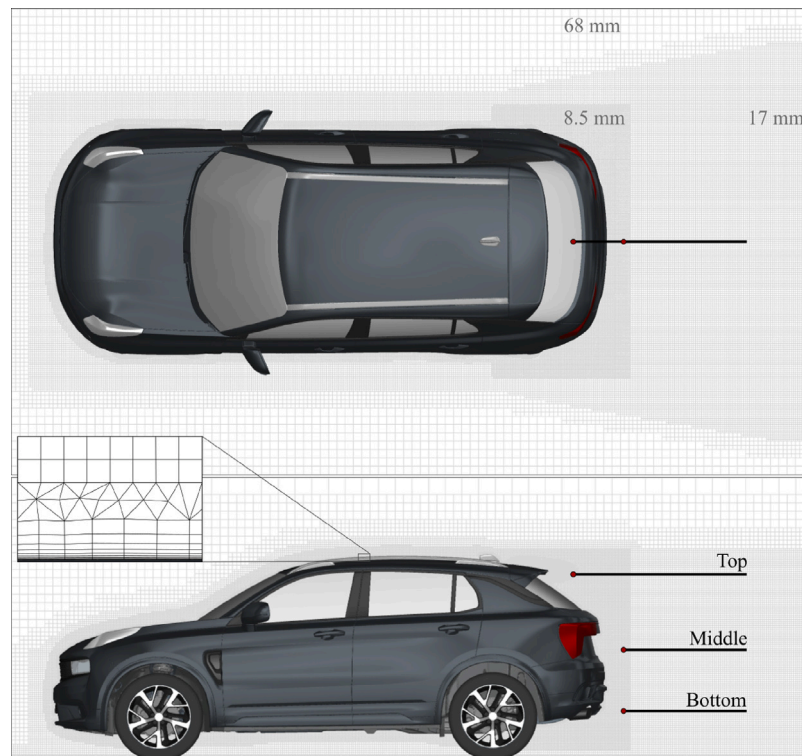
Table 2
Setup and results for the cell count investigation of the mesh study, using wind tunnel results as reference.

Mesh size	Cell count	Prism layers	Time step size [s]	$\Delta C_D^{5°}$	$\Delta C_{lf}^{5°}$	$\Delta C_{lr}^{5°}$	$\Delta \left(C_{lf} - C_{lr} \right)^{5°}$
Extra fine	237×10^6	17	1.6×10^{-4}	0.003	−0.028	−0.031	0.003
Fine	190×10^6	15	1.6×10^{-4}	0.000	−0.025	−0.021	−0.004
Medium	144×10^6	14	1.6×10^{-4}	−0.003	−0.030	−0.018	−0.013
Coarse	103×10^6	7	1.6×10^{-4}	0.000	−0.029	−0.046	0.017

Table 3
Setup and results for the time step investigation of the mesh study, using wind tunnel results as reference.

| Time step size [s]	Normalised time step size	Mesh size	$\Delta C_D^{5°}$	$\Delta C_{lf}^{5°}$	$\Delta C_{lr}^{5°}$	$\Delta \left(C_{lf} - C_{lr} \right)^{5°}$
0.8×10^{-4}	1269	Fine	−0.001	−0.027	−0.026	0.000
1.6×10^{-4}	635	Fine	0.000	−0.025	−0.021	−0.004
2.5×10^{-4}	406	Fine	0.003	−0.026	−0.023	−0.004
5.0×10^{-4}	203	Fine	0.006	−0.027	−0.024	−0.003

Fig. 3. The fine mesh showing the zone refinements around the vehicle, a zoom in of the prism layers, and the two-point correlation lines.

2.3.2. Time step size

Four time step sizes were investigated using the fine mesh, see Table 3. Ekman et al. (2019) defined the normalised time step size as the number of time steps needed for the freestream to travel the length of the vehicle. They concluded that a value above 400 or higher is preferred. In this work, the best results were seen using the two smallest time steps, although the solution was not particularly sensitive to larger time steps. The results in Table 3, the recommendations by Ekman et al. (2019) and the available computational resources led to the use of a time step size of 1.6×10^{-4} s in this study.

2.3.3. Two-point correlation

The mesh accuracy was further evaluated by analysing the mesh quality in the wake behind the vehicle, using two-point correlation of the longitudinal velocities along the three lines displayed in Fig. 3. Two-point correlation has been proposed by Davidson (2009) as a better alternative when evaluating LES resolution compared to, e.g., energy spectra and resolved turbulent kinetic energy and has been used in previous studies (Urquhart et al., 2018; Ljungskog et al., 2020; Törnell et al., 2021; Josefsson et al., 2022). The normalised two-point
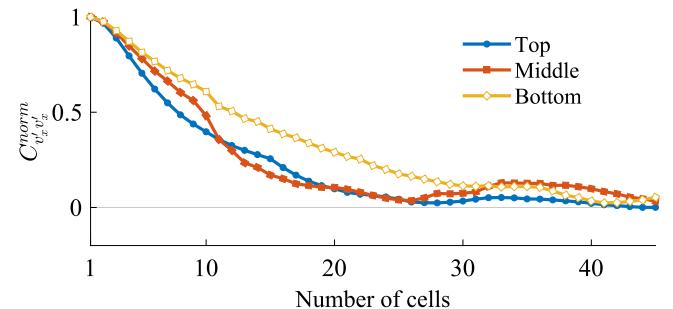
Fig. 4. The two-point correlation results.

correlation (Eq. (1)) between spatial coordinates x_A and x_B gives a value close to unity when the signals are highly correlated and close to zero for uncorrelated signals. Each line in Fig. 3 has its reference point x_A (red dot) located furthest towards the vehicle. The number of
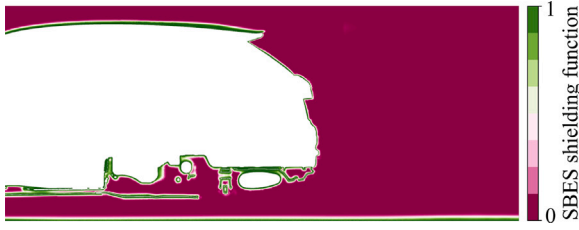
Fig. 5. Shielding function of SBES, showing regions of LES (purple) and RANS (green). (For interpretation of the references to colour in this figure legend, the reader is referred to the web version of this article.)

Fig. 6. Base probes used for creating vertical and lateral base pressure gradients.

correlated cells along a line in a separated region indicates how well the mesh can resolve the turbulent structures. According to Davidson (2009), at least eight cells should be correlated in LES to properly resolve the largest eddies. As seen in Fig. 4, all lines fulfilled this criterion.

$$C_{v_x' v_x'}^{norm}\left(x_A, x_B\right) = \frac{\overline{v_x'\left(x_A\right) v_x'\left(x_B\right)}}{v_{x,rms}\left(x_A\right) v_{x,rms}\left(x_B\right)} \tag{1}$$

The high quality of the mesh was further affirmed by analysing the switching between RANS at the wall to the LES formulation outside the boundary layer where the grid resolution allows it. Fig. 5 shows that most of the flow around the vehicle is resolved with the LES formulation, while the thin boundary layers at the vehicle and ground are modelled with RANS, as expected.

2.4. Post-processing

2.4.1. Aerodynamic coefficients

The aerodynamic coefficients were determined by normalising the forces and moments with the density of air, ρ, vehicle speed, v_x, frontal area, A, and wheel base, L, (for the moments). Similarly, the pressure coefficient, C_p, was determined by normalising the pressure difference to the freestream pressure, $p - p_s$, with the dynamic pressure without crosswind (see Eq. (2)).

$$C_{\text{force}} = \frac{\text{force}}{\frac{1}{2}\rho A v_x^2}, \qquad C_{\text{moment}} = \frac{\text{moment}}{\frac{1}{2}\rho A L v_x^2}, \qquad C_p = \frac{p - p_s}{\frac{1}{2}\rho v_x^2} \tag{2}$$

2.4.2. Base pressure gradients

Aspects of wake dynamics such as up- or down-wash dominated wakes can be traced on the transient base pressures. Commonly used quantities for wake stability are the vertical and lateral base pressure gradient. The base pressure gradient can be constructed by monitoring the transient base pressures on several positions at the rear (similar to an experimental setup), see Fig. 6, and creating a non-dimensional vertical base pressure gradient, $\frac{\partial c_p}{\partial z^*}$, between the top and bottom probes, see Eq. (3). Similarly, the lateral non-dimensional base pressure gradient, $\frac{\partial c_p}{\partial y^*}$, was calculated from the difference between the left and right side probes, Eq. (4). Where the distances z^* and y^* were non-dimensionalised with the track width, W. The top, bottom, left and right probes were spatially averaged as in Eq. (5), where n_c and n_r represent the number of columns and rows, respectively, and i is the indexing of the probe in the row or column.

$$\frac{\partial c_p}{\partial z^*}(t) = \frac{c_p^{top}(t) - c_p^{bottom}(t)}{\delta_z / W} \tag{3}$$

$$\frac{\partial c_p}{\partial y^*}(t) = \frac{c_p^{left}(t) - c_p^{right}(t)}{\delta_y / W} \tag{4}$$

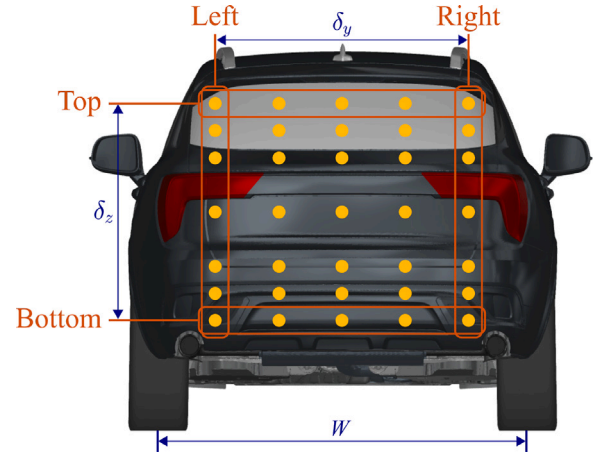$$c_p^{top}(t) = \frac{1}{n_c} \sum_{i=1}^{n_c} c_p\left(y_i, z_{top}, t\right)$$

$$c_p^{bottom}(t) = \frac{1}{n_c} \sum_{i=1}^{n_c} c_p\left(y_i, z_{bottom}, t\right)$$

$$c_p^{left}(t) = \frac{1}{n_r} \sum_{i=1}^{n_r} c_p\left(y_{left}, z_i, t\right)$$

$$c_p^{right}(t) = \frac{1}{n_r} \sum_{i=1}^{n_r} c_p\left(y_{right}, z_i, t\right) \tag{5}$$

2.5. Vehicle dynamic coupling

The aerodynamic loads (forces and moments) were applied to a vehicle dynamic model to investigate their effect on driving stability. The loads were applied in a 1-way coupling, meaning that the aerodynamics affected the vehicle dynamic motion response, but this motion was not accounted for in the aerodynamic simulations. A 2-way coupling of the lateral motion was previously proven unnecessary for passenger vehicles when evaluating crosswind sensitivity (Brandt, 2021). Furthermore, it can be shown that the vertical vehicle motion caused by the aerodynamic fluctuations is within 1% of the total ground clearance for the vehicle used in this study. This means that using a 2-way coupling would not significantly change the underbody flow nor the results presented here. Therefore, the more cost-efficient 1-way coupling was used. The vehicle dynamic model was based on the framework of the *enhanced* model, developed for crosswind sensitivity analysis in Brandt et al. (2021). The enhanced model included 3 degrees of freedom (lateral, yaw and roll dynamics) and accounts for the suspension system's kinematic and elasto-kinematic steering effects. In the present work, vertical (heave and pitch) and longitudinal dynamics were added to evaluate the effects of the aerodynamic lift and drag forces. The vertical suspension stiffness and damping were modelled for each axle. Hence, this vehicle dynamic model had 6 degrees of freedom.

The simulation setup included a driver model that found the fixed steering wheel angle for driving in a straight path when applying the time-averaged aerodynamic loads for the various flow angles. The fixed steering wheel angle was kept constant when the transient aerodynamic loads were applied to the model. Hence, there were no steering interventions during the transient load. Although this driver model is quite simplified, the scenario of driving at highway speeds in a straight line implies little steering input from the driver. Therefore, it was expected that this would be sufficient to assess the differences between roof spoilers under constant crosswind conditions.
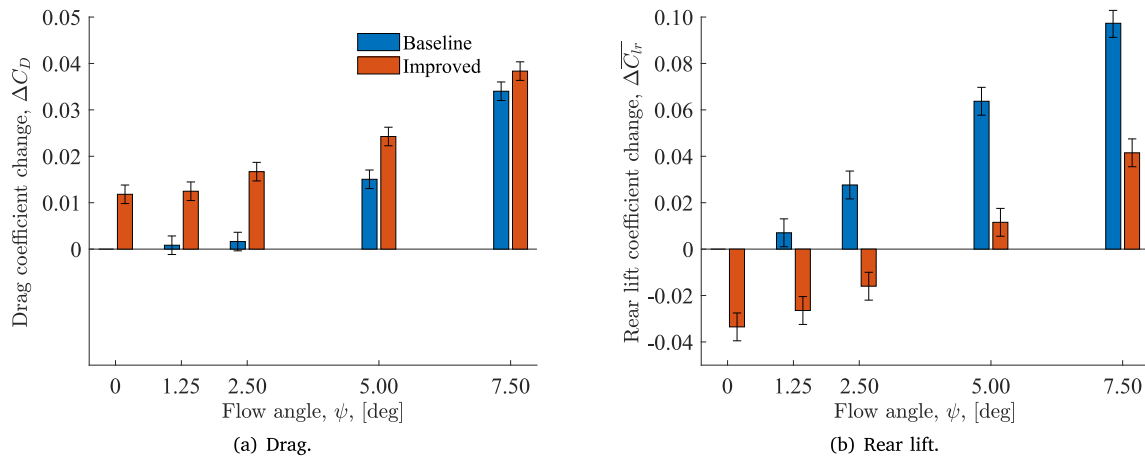
(a) Drag.

(b) Rear lift.

Fig. 7. The influence of spoiler design and yawed flow angle on the aerodynamic coefficients, with the baseline spoiler at zero flow angle as reference. Uncertainties were estimated based on averaging time, and the mesh and time step study.
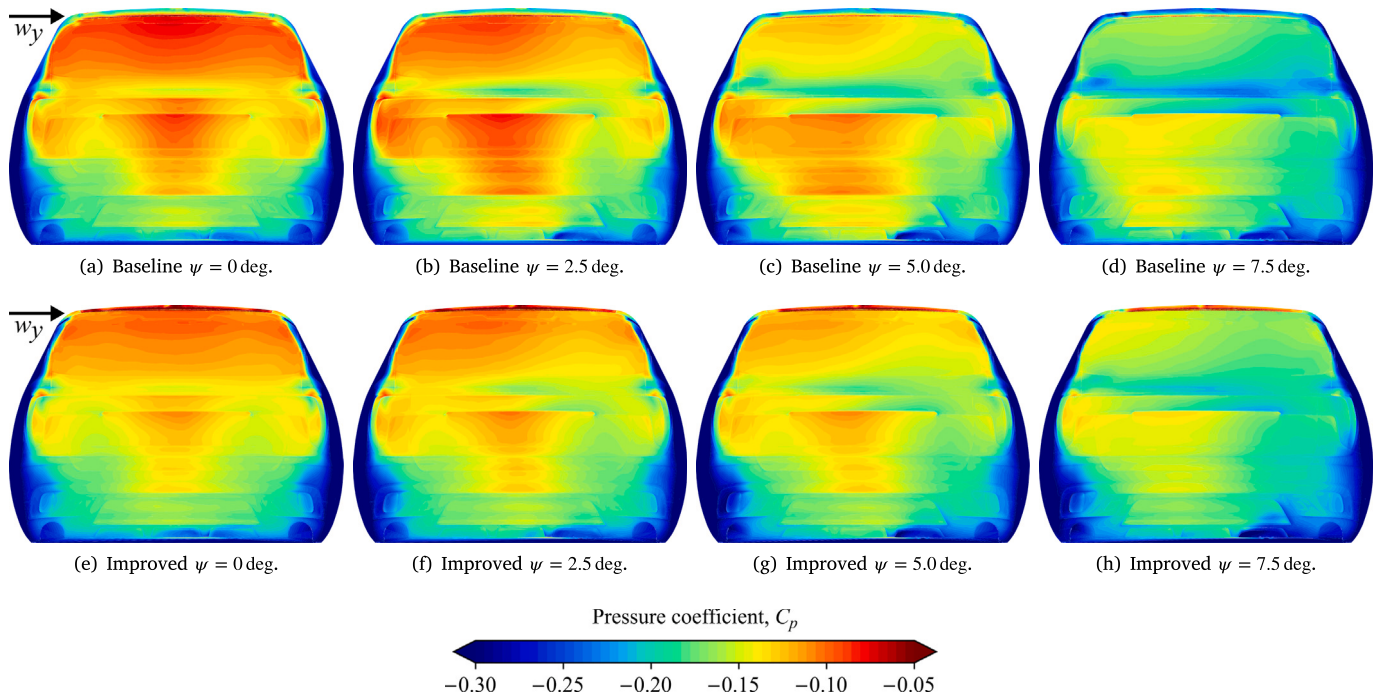

(a) Baseline $\psi = 0$ deg. (b) Baseline $\psi = 2.5$ deg. (c) Baseline $\psi = 5.0$ deg. (d) Baseline $\psi = 7.5$ deg.

(e) Improved $\psi = 0$ deg. (f) Improved $\psi = 2.5$ deg. (g) Improved $\psi = 5.0$ deg. (h) Improved $\psi = 7.5$ deg.

Pressure coefficient, C_p

$-0.30 \quad -0.25 \quad -0.20 \quad -0.15 \quad -0.10 \quad -0.05$

Fig. 8. Time-averaged base pressure coefficient, $\overline{C_p}$, for the two spoilers at 0, 2.5, 5 and 7.5 deg yawed flow angle.

3. Results

The aerodynamic performance related to driving stability will be compared for the two rear roof spoilers, in terms of time-averaged and unsteady time-dependent quantities. An analysis of the wake dynamics is then conducted to highlight some valuable insights on the high speed stability performance of the spoilers. Finally, the vehicle dynamic effects from these unsteady aerodynamic loads will be presented.

3.1. Influence of spoiler design and flow angle

The baseline and improved spoilers (Figs. 1(b) and 1(c)) were investigated at five angles of constant yawed flow. The averaged force and flow data obtained from the unsteady CFD simulation are presented first, to show the overall aerodynamic characteristics of the vehicle with its two spoilers. Then, the emphasis of this study will be put on

the unsteady force and flow data, investigating the base wake dynamics and its influence on the aerodynamic loads.

3.1.1. Averaged forces, base pressures and flow fields

When evaluating the aerodynamic performance of a vehicle, the time-averaged forces are discussed and compared primarily. The time-averaged delta drag and rear lift coefficients, $\overline{C_D}$ and $\overline{C_{lr}}$, between the two spoilers at various yaw angles are presented in Fig. 7, with the baseline spoiler at 0 deg yawed flow as reference. Analysing the drag (Fig. 7(a)), shows that the improved spoiler has increased the drag at all flow angles. However, the baseline design is more sensitive, in terms of drag, to yawed flow. The improved spoiler decreased the rear lift compared to the baseline at all yaw angles, see Fig. 7(b). This rear lift offset between spoilers increases slightly for larger flow angles. The other time-averaged forces and moments were relatively unaffected by the geometric design change and are therefore not presented here.
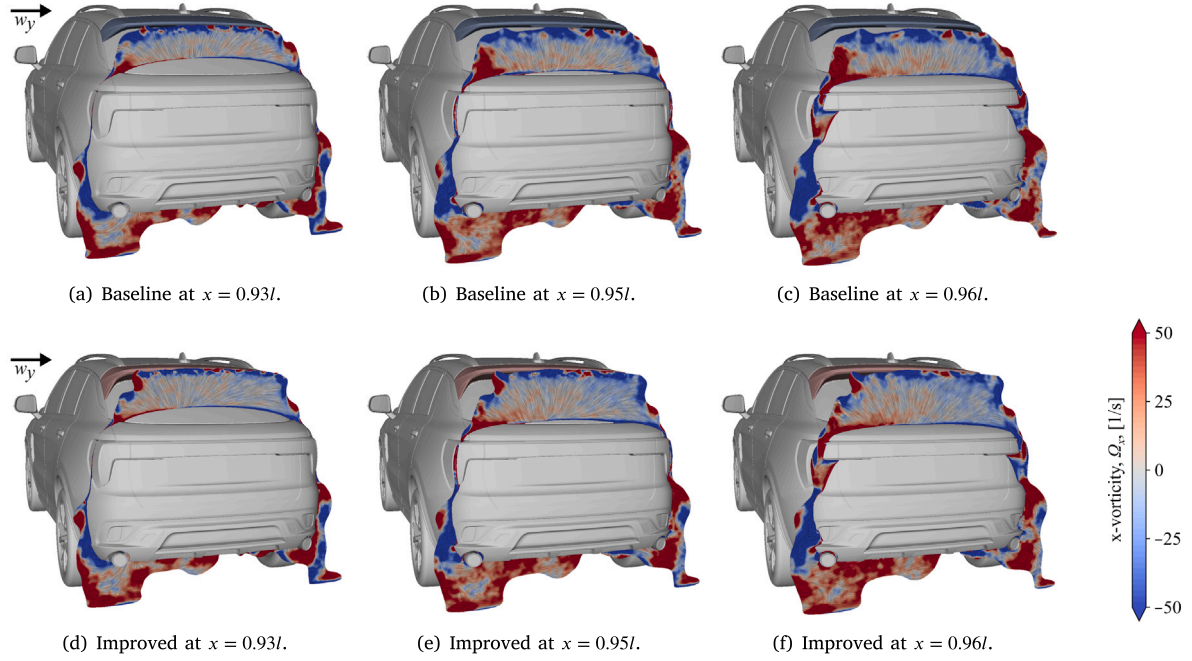
(a) Baseline at $x = 0.93l$.

(b) Baseline at $x = 0.95l$.

(c) Baseline at $x = 0.96l$.

(d) Improved at $x = 0.93l$.

(e) Improved at $x = 0.95l$.

(f) Improved at $x = 0.96l$.

Fig. 9. The time-averaged vorticity in x-normal planes, at 5 deg yawed flow. The values are clipped where the total pressure coefficient is larger than 0.
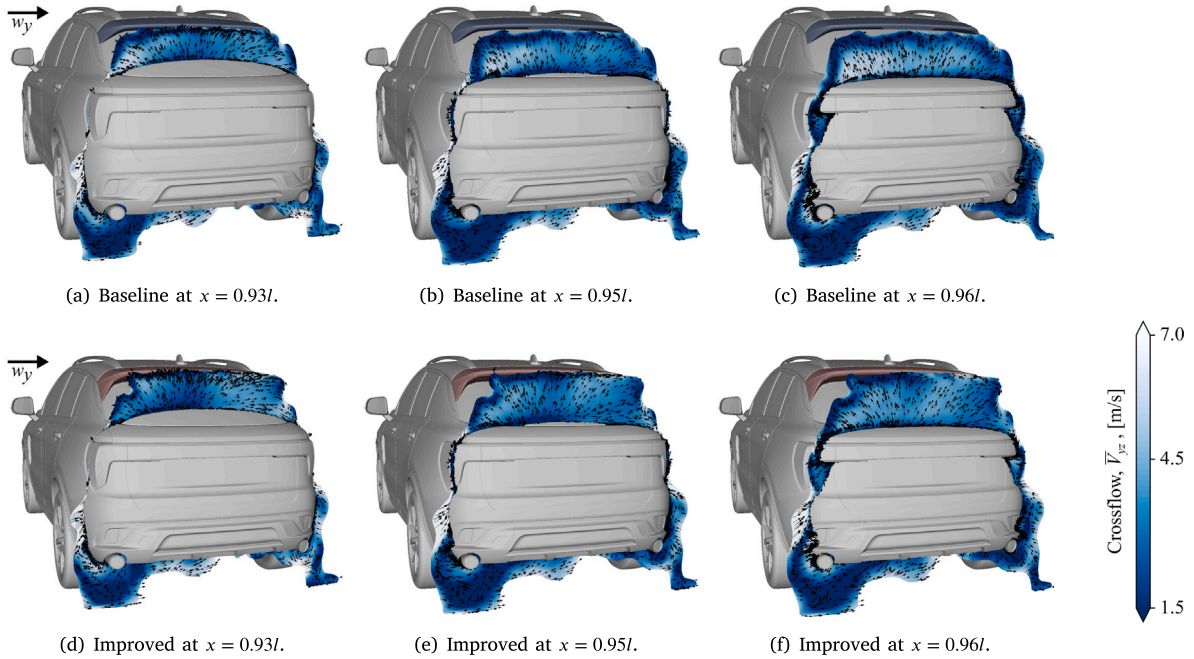

(a) Baseline at $x = 0.93l$.

(b) Baseline at $x = 0.95l$.

(c) Baseline at $x = 0.96l$.

(d) Improved at $x = 0.93l$.

(e) Improved at $x = 0.95l$.

(f) Improved at $x = 0.96l$.

Fig. 10. The time-averaged crossflow with velocity vectors in x-normal planes, at 5 deg yawed flow. The values are clipped where the total pressure coefficient is larger than 0.

The time-averaged base pressures in Fig. 8 reflect what was observed in Fig. 7(a). A higher base pressure is seen for the baseline (Fig. 8(a)–8(d)) compared to the improved spoiler (Fig. 8(e)–8(h)), explaining the higher drag for the latter. Its more aggressive kick creates a larger wake with even more up-wash, reducing the base pressure at small flow angles. When increasing the flow angle, a considerable pressure reduction is seen on the slanted rear windscreen, going from 2.5 deg to 5 deg flow angle for the baseline spoiler (Figs. 8(b) and 8(c)) and additionally at 7.5 deg (Fig. 8(d)). The improved spoiler design shows a relatively smaller pressure loss on the rear windscreen between 2.5 deg to 5 deg flow angle (Figs. 8(f) and 8(g)) and even higher pressure on the rear windscreen at 7.5 deg (Fig. 8(h)) compared to the baseline

spoiler. Furthermore, the improved spoiler has the high pressure zone located further towards the top of the base, indicating a more up-wash dominated wake and thus lower rear lift.

The base pressure differences between the spoiler designs can be further understood by analysing time-averaged flow quantities at the base, especially near the rear windscreen. Figs. 9 and 10 show the vorticity, Ω_x, and crossflow, $\overline{V}_{yz}$, in x-normal planes located at 93 %, 95 % and 96 % of the vehicle length, for the 5 deg yawed flow condition. The planes are clipped where the total pressure is larger than 0, to indicate the wake size. As mentioned, the more aggressive kick angle of the improved spoiler creates a taller wake. The flow around the lower half of the vehicles looks almost identical, as expected when comparing
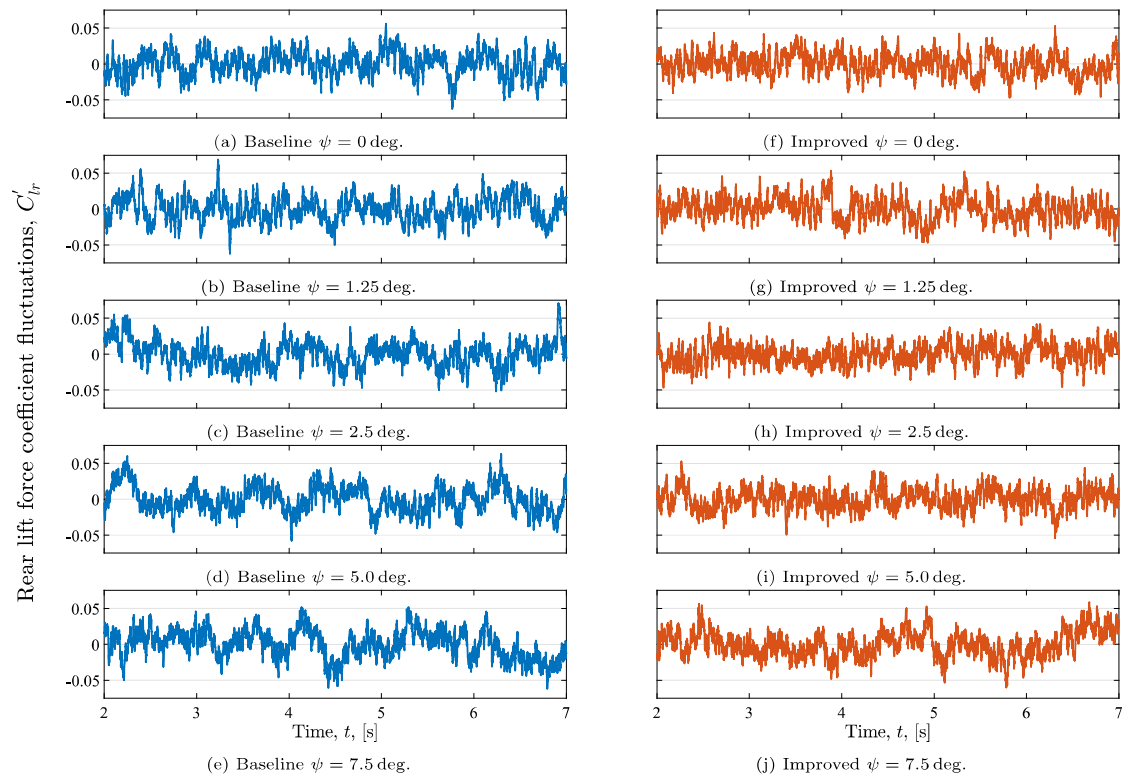
Fig. 11. Rear lift fluctuations ($C'_{lr} = C_{lr} - \overline{C_{lr}}$) for the two spoilers at 0, 1.25, 2.5, 5 and 7.5 deg yawed flow angle.
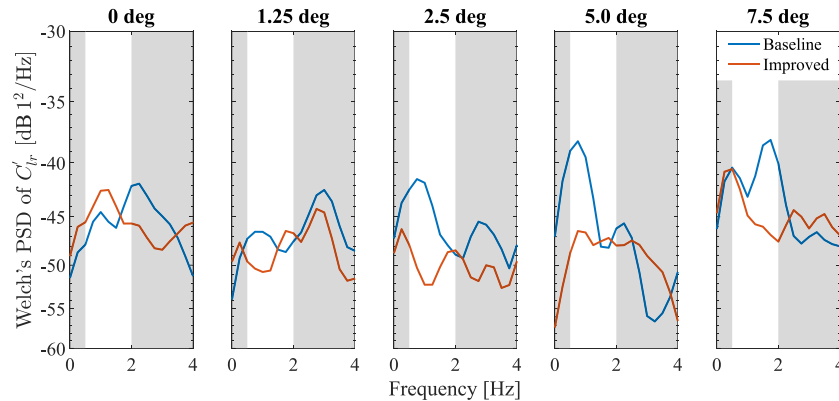

Fig. 12. Welch's PSD (power spectral density) frequency response of the rear lift fluctuations ($C'_{lr} = C_{lr} - \overline{C_{lr}}$) for the two spoilers at 0, 1.25, 2.5, 5 and 7.5 deg yawed flow angle. Using 2 s window size and 90% overlap.

the two spoilers, while the flow behaviour at the upper part shows notable differences. The baseline configuration creates a strong anti-clockwise vortex structure (positive vorticity). The up-wash of the wake generate some out-flow at the mid-to-upper part of the inclined rear windscreen while the in-flow from the windward side occur further down on the lower part of the windscreen and on the boot lid. The improved spoiler weakens this structure and creates several smaller counter-rotating vortices. Furthermore, a clockwise vortex structure (negative vorticity) can be observed on the lower leeward side of the rear windscreen for the baseline (Fig. 10(c)) but not as strong for the improved configuration (Fig. 10(f)). Both these vortex structures could be traced on the base pressure as zones of lower pressure on the lower outer parts of the rear windscreen in Fig. 8(c).

Fig. 10 shows the in-plane crossflow magnitude. The crossflow magnitude is lower for the improved spoiler, especially at the windward side of the rear windscreen. The baseline spoiler shows noticeably larger crossflow magnitudes in this region where the in-flow at the

beginning of the bot lid can be observed along with the outflow at the mid-to-upper part of the rear windscreen, as discussed above. The reduced crossflow, the absence of strong vortex structures and the more up-wash dominated wake of the improved spoiler design explain its higher rear windscreen base pressure seen in Fig. 8(g), compared to the baseline in Fig. 8(c). However, these time-averaged results mask any transient phenomena that might affect the driving stability performance. These effects will be discussed next.

3.1.2. Unsteady forces

The rear lift fluctuations ($C'_{lr} = C_{lr} - \overline{C_{lr}}$) are presented in Fig. 11, for the two spoilers in five yawed flow conditions. The vehicle equipped with the baseline spoiler experienced higher amplitudes of fluctuations close to 1 Hz, compared to the improved spoiler. This is especially evident at flow angles of 5.0 and 7.5 deg. These time-series results can be analysed in the frequency domain, using Welch's windowing method for power spectral density (PSD) analysis. Fig. 12 shows the PSD of
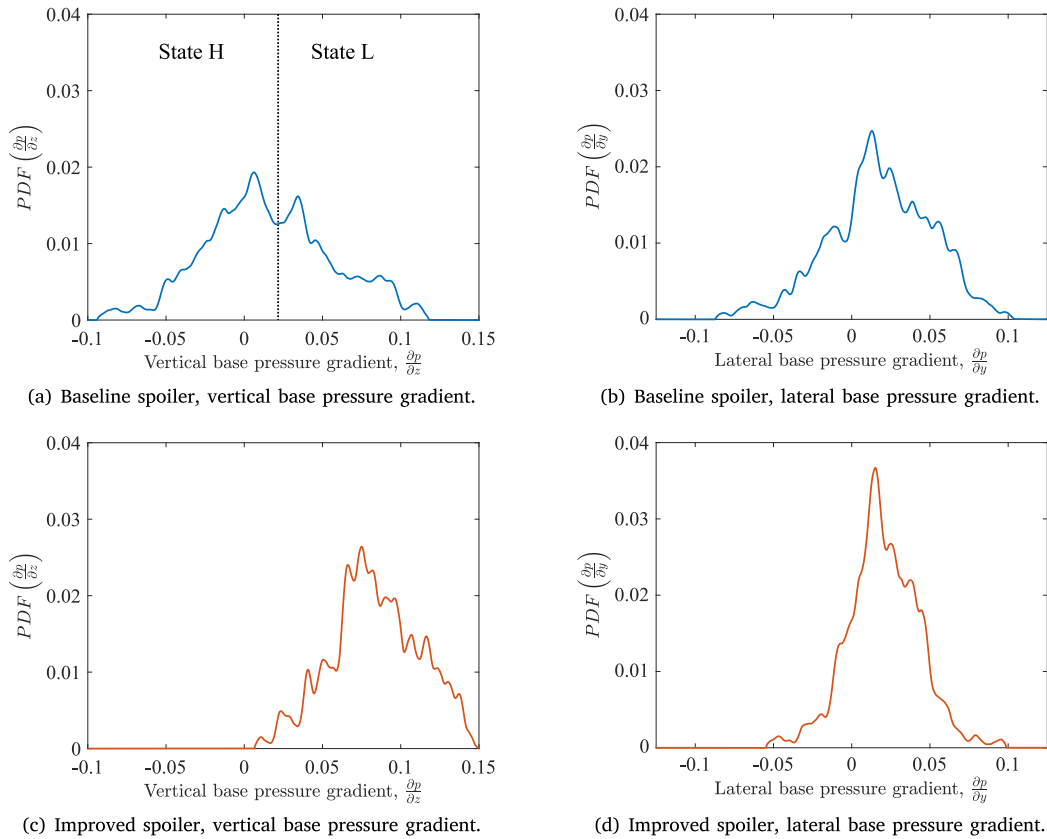
(a) Baseline spoiler, vertical base pressure gradient.

(b) Baseline spoiler, lateral base pressure gradient.

(c) Improved spoiler, vertical base pressure gradient.

(d) Improved spoiler, lateral base pressure gradient.

Fig. 13. Average shifted histograms of the base pressure gradients (vertical and lateral) for two spoiler at $5\,\text{deg}$ yawed flow.

the rear lift fluctuations in the frequency range of $0\,\text{Hz}$ to $4\,\text{Hz}$, with a highlighted focus on $0.5\,\text{Hz}$ to $2\,\text{Hz}$ known as a sensitive range for the vehicle dynamics. Note that negative PSD values can occur since decibel (dB) is a relative logarithmic measure. Hence, the relative difference between values should only be considered, not the absolute values. The improved spoiler has consistent frequency response levels for all flow angles, except a higher response at $0.5\,\text{Hz}$ for the $7.5\,\text{deg}$ yawed flow case. At 0 and $1.25\,\text{deg}$, the baseline spoiler had a similar frequency response, but higher amplitude fluctuations for larger flow angles. The largest difference happens at $5\,\text{deg}$ flow angle, where the improved spoiler managed to keep the frequency response to similar levels as for the smaller flow angles, while the baseline configuration generated large low-frequency fluctuations close to $1\,\text{Hz}$. The implications of these low-frequency fluctuations will be analysed further in Section 3.3, where vehicle dynamic effects will be discussed and related to the real driving stability performance. The flow dynamics causing these fluctuations are of great interest for understanding and possibly preventing this phenomenon. This will be discussed below.

3.2. Base wake dynamics

This section presents an analysis of the base wake using the base pressure gradient and conditional averaging of low and high lift modes for base pressure, skin friction and flow field, for the two spoilers and the $5\,\text{deg}$ yawed flow angle. This angle was chosen as it displayed the largest low-frequency differences between the two spoilers.

3.2.1. Base pressure gradient

Pressure gradients on the base were calculated using Eqs. (3) and (4) in the vertical and lateral directions, respectively. These time-dependent gradients can be plotted as probability density functions (PDF) to visualise the variance in the data and to determine if there are more than one state in the wake dynamics. In Fig. 13(a), it can

be observed that there are two peaks of higher probability compared to the vertical base pressure value of the dashed line between the peaks. This indicates that there exist two dominant wake flow states for the baseline spoiler at $5\,\text{deg}$, which can be linked to the large low-frequency fluctuations discussed in Fig. 11. The states H and L represent wake dynamics that generate high versus low rear lift forces, respectively. The corresponding data for the improved spoiler can be seen in Fig. 13(c). Only one flow state is observed, using this method of analysis, and it is evident that the improved spoiler creates a higher vertical base pressure gradient (indicating more up-wash and lower rear lift) with less variance.

Figs. 13(b) and 13(d) shows the PDF:s of the lateral base pressure gradients. Only one state is present for both spoilers. However, the baseline spoiler has a greater variance compared to the improved spoiler. This means that the centre of pressure also moves more laterally using the baseline spoiler, possibly affecting the lateral dynamics of the vehicle.

3.2.2. Conditionally averaged base pressure and skin friction modes

To analyse the wake characteristics of the two states in Fig. 13(a), a conditional averaging approach was utilised, based on the value of the rear lift force signal. When the rear lift was above its 75th percentile value, all unsteady base pressure, skin friction and flow field data were stored and averaged in a high (H) lift mode variable and similarly for the low (L) lift mode below the 25th percentile. The 75th and 25th percentiles were chosen to capture the wake modes at the high and low amplitudes of the low frequency fluctuations observed in Figs. 11 and 12.

The two modes of the base pressure coefficient for the baseline spoiler can be seen in Fig. 14, which also corresponds to the vertical base pressure states in Fig. 13(a). The centre of pressure is located further down for the high rear lift mode. However, the largest difference between the two modes is observed in the pressure on the rear
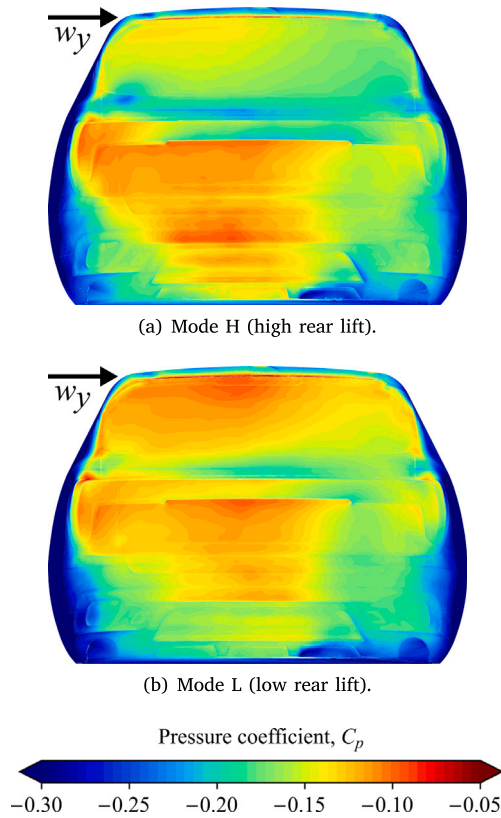
(a) Mode H (high rear lift).

(b) Mode L (low rear lift).

Pressure coefficient, C_p

$-0.30 \quad -0.25 \quad -0.20 \quad -0.15 \quad -0.10 \quad -0.05$

Fig. 14. Conditionally averaged base pressures for the high (H) and low (L) rear lift modes, for the baseline spoiler at 5 deg yawed flow.

(a) Time-averaged.

(b) Difference between mode H and L.

Fig. 15. Time-averaged skin friction coefficient, C_f, and the difference between high (H) and low (L) rear lift modes, for the baseline spoiler at 5 deg yawed flow. (For interpretation of the references to colour in this figure legend, the reader is referred to the web version of this article.)

(a) Baseline.

(b) Improved.

Pressure coefficient difference, ΔC_p

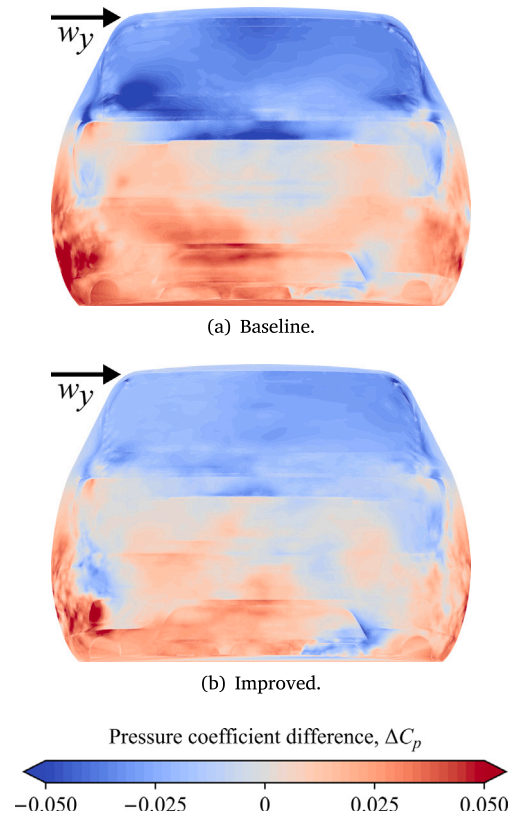$-0.050 \quad -0.025 \quad 0 \quad 0.025 \quad 0.050$

Fig. 16. Conditionally averaged base pressures difference between the high (H) and low (L) rear lift modes, for the two spoilers at 5 deg yawed flow.
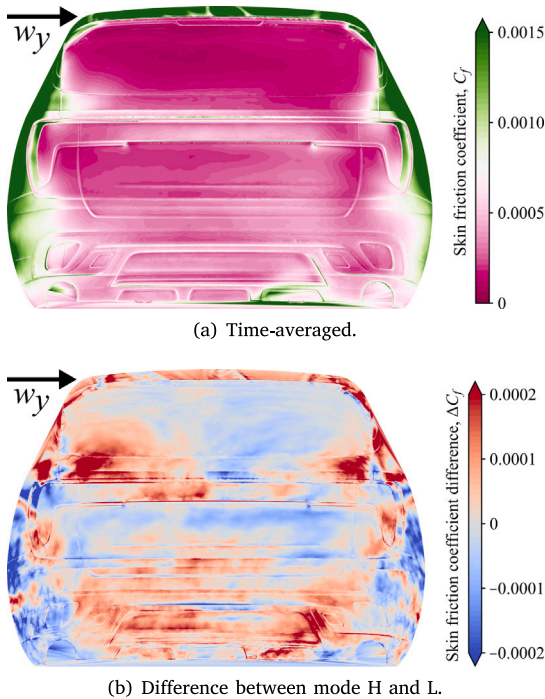
windscreen and beginning of the boot lid, where the high lift mode shows a local low-pressure zone on the lower windward side of the rear windscreen. This zone is caused by the vortex structure seen in Fig. 10(c) temporarily attaching in this location at high lift modes. The low lift mode has a higher rear windscreen pressure, resembling the averaged values at smaller flow angles in Fig. 8, while the high lift mode shows considerably lower rear windscreen pressure.

To analyse flow attachment, the skin friction coefficient, C_f, is plotted in Fig. 15(a). High skin friction (green) indicates attached flow, while nil or small (purple) indicates regions of separated flow. As expected, there is a clear separation over the roof spoiler, and a gradual shift from high to low skin friction around the sides of the base, implying that there is no clear separation edge on the side radii and that the line of separation varies in time. At the lower outer sides of the rear windscreen, a medium level (white) of the time-averaged skin friction is shown, agreeing with the conclusion of a detaching and re-attaching structure. This is further highlighted in Fig. 15(b), where the difference in skin friction coefficient, ΔC_f, between the high and low lift modes is presented. The high rear lift mode has higher skin friction at the lower outer parts of the rear windscreen, indicating that the attached vortex structure was only present for this mode.

The vehicle equipped with the improved spoiler also has a fluctuating rear lift force. By creating similar high and low lift modes using the 25th and 75th percentile values, a comparison to the baseline spoiler could be created, see Fig. 16. The general trend of a high lift mode with lower pressure on the upper half of the base and higher pressure on the lower half is seen for both spoilers. Nevertheless, the pressure difference between the upper and lower half is greater for the baseline spoiler. More noticeably, the baseline spoiler has, as seen above, a low pressure zone on the windward side of the rear windscreen at its high lift mode. This cannot be observed with the improved
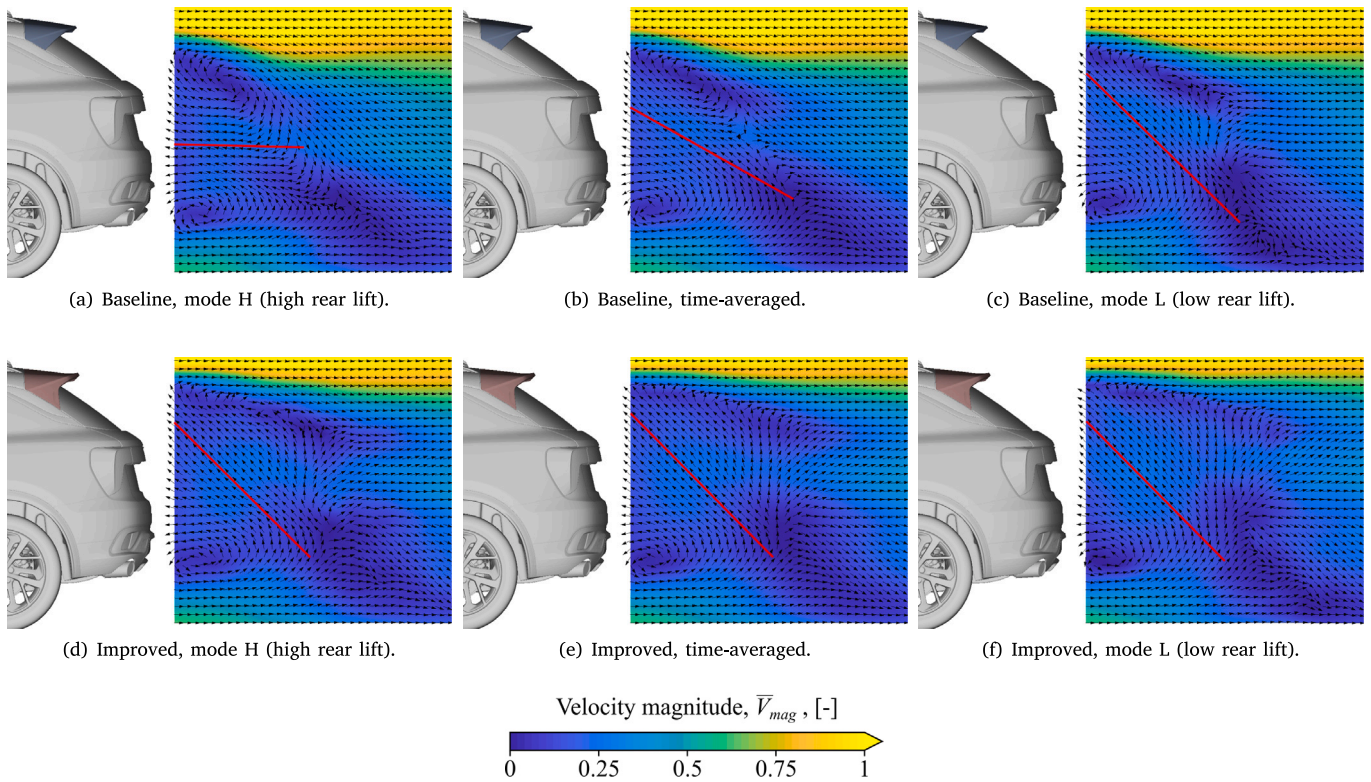
(a) Baseline, mode H (high rear lift). (b) Baseline, time-averaged. (c) Baseline, mode L (low rear lift).

(d) Improved, mode H (high rear lift). (e) Improved, time-averaged. (f) Improved, mode L (low rear lift).

Velocity magnitude, $\overline{V}_{mag}$, [-]

0   0.25   0.5   0.75   1

Fig. 17. Conditionally averaged wake velocity fields for the high (H) and low (L) rear lift modes, for the two spoilers at 5 deg yawed flow. Additionally, the time-averaged velocity fields are included for comparison in the y-normal centreline planes. The red lines are manually positioned in the overall flow direction towards the base, to mark the wake balance.

spoiler. The up-washed design of the improved spoiler, with higher base pressure gradient and windscreen pressure, seems to counteract the vortex structures forming when the flow separates past the sides of the slanted rear windscreen, and prevents re-attachment on the rear windscreen. A down-washed designed roof spoiler will strengthen the vortex structure and may lead to re-attachment at the lower part of the rear windscreen, as for the baseline spoiler.

3.2.3. Conditionally averaged flow field modes

The conditional averaging methodology was also used to analyse the flow dynamics in the wake. Fig. 17 shows the velocity magnitude at the centreline in 5 deg yawed flow for the two spoilers, where the red lines are manually positioned in the overall flow direction towards the base to qualitatively mark the wake balance. The time-averaged velocities are presented in Figs. 17(b) and 17(e), where the improved spoiler creates a taller and more up-washed wake. The increased wake size aligns with the higher drag discussed in Section 3.1.1. Interestingly, the improved spoiler's high and low lift modes show similar up-washed wake characteristics as its time-averaged data, indicating a relatively stable wake. In comparison, the baseline spoiler shows a balanced wake for its high lift mode (Fig. 17(a)) and an up-washed dominated low lift mode (Fig. 17(c)), similar to the wake of the improved spoiler. The vortex structures attaching at the lower outer sides of the rear windscreen for the baseline spoiler correspond to the balanced wake of high rear lift. The switching between balanced (mode H) and up-wash dominated wake (mode L) does not only affect the pressure at the base, but also the underbody and exterior flow. It is these large wake motions that cause the large fluctuations in the aerodynamic rear lift force discussed in Figs. 11 and 12.

3.3. Vehicle dynamic effects on low-frequency rear lift fluctuations

The unsteady aerodynamic loads were applied to the vehicle dynamic model described in Section 2.5. The lift forces will directly influence the normal loads at the tyres and, consequently, the cornering stiffness at the front and rear axles. The variations in rear axle cornering stiffness due to the unsteady aerodynamics can be seen in Fig. 18. Fig. 18 show the results when modelling the vehicle as stiff, i.e. without any vertical dynamics. It is evident that the rear lift force fluctuations are transmitted to affect the cornering stiffness values. The baseline spoiler shows the same low-frequency fluctuations, whereas the improved spoiler fluctuates closer to the average value. Interestingly, when modelling the vertical dynamics of the vehicle with the axle spring and damper stiffnesses, the high frequency fluctuations were reduced by the spring–damper system, while the low-frequency fluctuations increased, see Fig. 18. This, since the 1st natural frequency of the rear suspension lies closely to the aerodynamic low-frequency fluctuations, thus intensifying the effect. The variations in cornering stiffness were smaller for the improved spoiler. Furthermore, its fluctuations of highest amplitude were closer to 2 Hz, compared with the high amplitude fluctuations of 1 Hz of the baseline spoiler configuration.

The comparison in Fig. 18 only included the two spoiler configurations at $\psi = 5$ deg flow angle. The cornering stiffness variation effect over a wide range of flow angles is presented in Fig. 19. The variation of the data between the 25th and 75th percentiles are shown in opaque colours, and the data between the 5th and 95th percentiles are presented in transparent colours, for the flow angle of 0, 1.25, 2.5, 5, 7.5, 10 and 15 deg. This, to indicate the cornering stiffness variations, in general and in maximum terms. Firstly, it can be noted that the improved spoiler shows smaller variations for all flow angles investigated, both in general and maximum terms. Furthermore, the general variation of the improved spoiler was fairly independent on flow angle, while the baseline spoiler generated the highest variations at 7.5 and 15 deg flow angles. Finally, a maximum variation of up to ±2 % was seen for the baseline spoiler. Naturally, a lower time-averaged rear axle lift force would be beneficial using this ratio measure. Nevertheless,
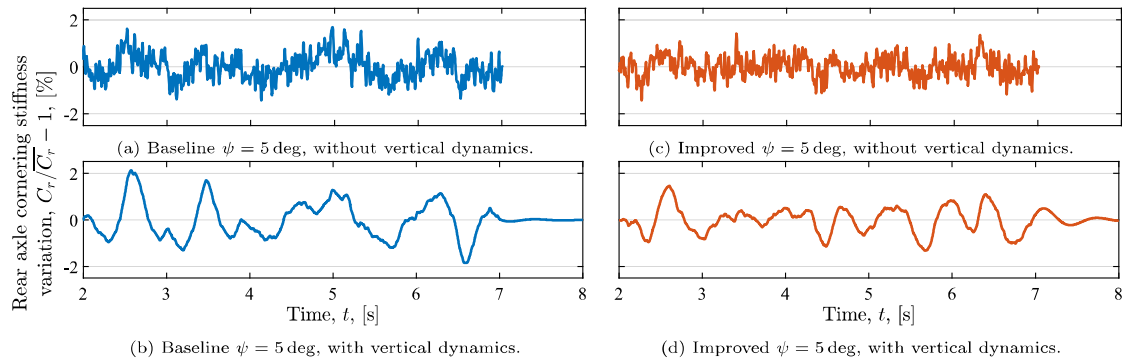
Fig. 18. The cornering stiffness variations for the two spoilers at $\psi = 5\,\mathrm{deg}$, with and without modelling the vertical dynamics of the vehicle.
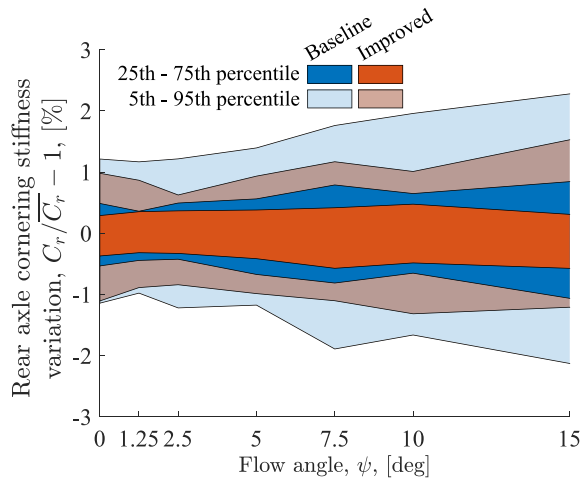

Fig. 19. The cornering stiffness variations for the two spoilers at $\psi = 0$, 1.25, 2.5, 5, 7.5, 10 and 15 deg. (For interpretation of the references to colour in this figure legend, the reader is referred to the web version of this article.)

Fig. 21. The yaw velocity variations for the two spoilers at $\psi = 0$, 1.25, 2.5, 5, 7.5, 10 and 15 deg. (For interpretation of the references to colour in this figure legend, the reader is referred to the web version of this article.)
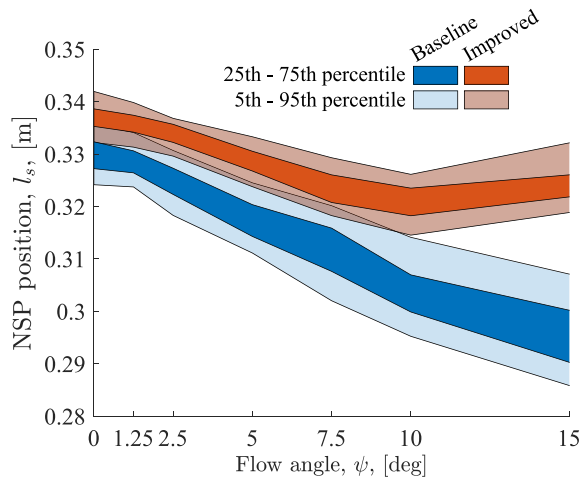

Fig. 20. The neutral steering point (NSP) variations, relative CoG, for the two spoilers at $\psi = 0$, 1.25, 2.5, 5, 7.5, 10 and 15 deg. (For interpretation of the references to colour in this figure legend, the reader is referred to the web version of this article.)

the effect from the lower average rear lift of the improved spoiler was approximately one order of magnitude smaller than the differences seen in the figure. The higher fluctuation amplitudes was, thus, the primary
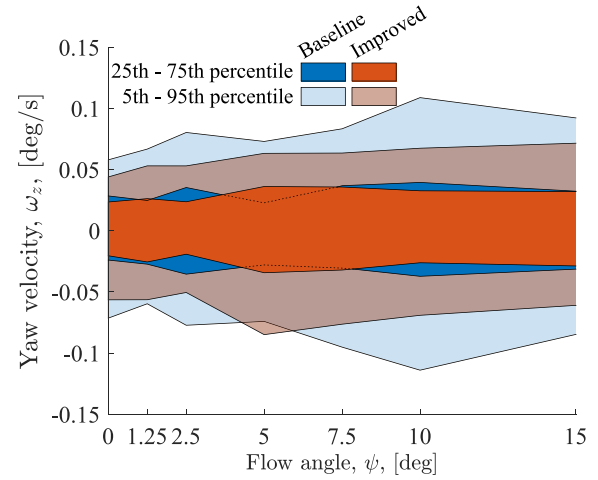
cause of the differences seen. The cornering stiffness at the rear axle is presented to directly show the effects of the different aerodynamic characteristics of the rear lift force. However, this is not, by itself, a measure that the driver can notice. The balance between the front and rear axle cornering stiffness determines the vehicle's understeering characteristics, which relates to the driver's perception of the vehicle. One measure of understeering is the distance, l_s, between the centre of gravity (CoG) and the neutral steering point (NSP). The NSP (also *tyre lateral force centre*) defines the position where a lateral force can be applied without initiating a yaw rotation. A larger distance l_s translates to more understeering. Fig. 20 shows the NSP position variations for the same flow angles. It is evident that the vehicle equipped with the improved spoiler yields more understeering at high speeds. Moreover, the baseline spoiler had an almost linearly decreasing understeering, as the flow angle increases, while the improved spoiler understeering was less sensitive to changes in flow angle. This means that the understeering characteristics of the baseline spoiler vary more at every set flow angle, but also that significant additional variations occur in conditions when the relative flow angle varies, which is the typical condition on the road.

Driving in crosswinds also generates lateral aerodynamic loads. This, with varying neutral steering point position, results in yaw velocity variations that might be interpreted as vehicle nervousness by the driver. Fig. 21 shows the yaw velocity variations, using a fixed steering wheel angle. There was no significant difference between the spoilers, for the general variations between the 25th and 75th percentiles. However, the maximum variations of the yaw velocity were higher for the baseline spoiler at almost all investigated flow angles.

4. Discussion

The common target on the time-averaged rear lift force is generally, by experience, an effective measure for designing vehicles with good driving stability performance. However, it might be that the primary benefit from this is that this target also tends to create more up-wash dominated and stable wakes, which reduces fluctuations of rear lift. This reduction in fluctuations might be more important than the secondary effect of increased time-averaged normal loads at the rear axle (which was only $\approx 100\,\text{N}$ higher for the improved spoiler at $160\,\text{km/h}$). Thus, when the requirements are set solely on averaged values, some vehicle designs can demonstrate poor stability performance due to unsteady base wake dynamics while still fulfilling the rear axle lift requirement. This would make the classical target setting insufficient and more effective requirements could be created by incorporating the unsteadiness of aerodynamics.

5. Conclusions

The wake dynamic effects on straight line high speed driving stability under yawed flow conditions have been investigated numerically for two variants of an SUV's roof spoiler: a baseline spoiler that was known to induce subjective stability issues and an improved spoiler that solved them. The numerical study was performed using unsteady aerodynamic flow simulations, with a one-way coupling to a vehicle dynamic model, to investigate the effects on handling. The analysis linked the unsteady wake dynamic effects and the rear lift force fluctuations with the handling characteristics of the vehicle.

The differences in spoiler geometry primarily affected the drag and rear lift forces, where the lift was of greater focus in this study. The baseline spoiler had higher base pressure at small flow angles and a pressure distribution that indicated less up-wash compared to the improved spoiler. The improved spoiler had lower base pressure, but could withstand higher flow angles before a large pressure reduction occurred on the rear windscreen, making it more robust for different flow angles. The analysis of the unsteady forces showed low-frequency ($0.5\,\text{Hz}$ to $2\,\text{Hz}$) rear lift fluctuations for the baseline spoiler, especially for larger flow angles, while the improved spoiler reduced the fluctuations at these frequencies. The vertical base pressure gradient indicated bi-stable wake dynamics for the baseline spoiler design. It was further concluded that this was coinciding with vortex structures occasionally re-attaching on the lower sides of the rear windscreen, during low windscreen pressure and inflow around the lower side radii of the windscreen, creating this bi-stable wake dynamics vertically. The up-washed design of the improved spoiler prevented this re-attachment of vortex structures, thus creating a more stable wake and reducing low-frequency lift fluctuations.

When coupling the aerodynamic load to the vehicle dynamic model, it was found that the vertical dynamics of the wheel suspension enhanced the normal load fluctuations at $1\,\text{Hz}$, since this lies close to the 1st natural frequency of the rear suspension. The improved spoiler showed smaller variations in rear axle cornering stiffness and an understeering characteristic less sensitive to variations in crosswind. This, together with slightly higher variations in yaw velocity when driving in crosswind conditions, led to the conclusion that these higher variations in handling characteristics most likely explain the baseline spoiler's lower subjective ratings of high speed driving stability compared to the improved spoiler.

CRediT authorship contribution statement

Adam Brandt: Conceptualization, Methodology, Software, Validation, Formal analysis, Investigation, Data curation, Writing – original draft, Visualization. **Simone Sebben:** Conceptualization, Methodology, Writing – review & editing, Supervision. **Bengt Jacobson:** Conceptualization, Methodology, Writing – review & editing, Supervision.

Declaration of competing interest

The authors declare that they have no known competing financial interests or personal relationships that could have appeared to influence the work reported in this paper.

Data availability

The authors do not have permission to share data.

References

Bonnavion, G., Cadot, O., Évrard, A., Herbert, V., Parpais, S., Vigneron, R., Délery, J., 2017. On multistabilities of real car's wake. J. Wind Eng. Ind. Aerodyn. 164, 22–33. http://dx.doi.org/10.1016/j.jweia.2017.02.004.

Bonnavion, G., Cadot, O., Herbert, V., Parpais, S., Vigneron, R., Délery, J., 2019. Asymmetry and global instability of real minivans' wake. J. Wind Eng. Ind. Aerodyn. 184, 77–89. http://dx.doi.org/10.1016/j.jweia.2018.11.006.

Brandt, Adam, 2021. Driving Stability of Passenger Vehicles under Crosswinds (Licentiate thesis). Chalmers University of Technology.

Brandt, Adam, Jacobson, Bengt, Sebben, Simone, 2021. High speed driving stability of road vehicles under crosswinds: an aerodynamic and vehicle dynamic parametric sensitivity analysis. Veh. Syst. Dyn. 1–24. http://dx.doi.org/10.1080/00423114.2021.1903516.

Brandt, Adam, Sebben, Simone, Jacobson, Bengt, Preihs, Erik, Johansson, Ingemar, 2020. Quantitative high speed stability assessment of a sports utility vehicle and classification of wind gust profiles. In: SAE Technical Paper Series. http://dx.doi.org/10.4271/2020-01-0677.

Buchheim, R., Maretzke, J., Piatek, R., 1985. The control of aerodynamic parameters influencing vehicle dynamics. SAE Paper 850279. http://dx.doi.org/10.4271/850279.

Cadot, O., Courbois, A., Ricot, D., Ruiz, T., Harambat, F., Herbert, V., Vigneron, R., Délery, J., 2016. Characterisations of force and pressure fluctuations of real vehicles. Int. J. Eng. Syst. Model. Simul. 8 (2), http://dx.doi.org/10.1504/ijesms.2016.075529.

Cooper, Kevin R., Watkins, Simon, 2007. The unsteady wind environment of road vehicles, part one: A review of the on-road turbulent wind environment. In: SAE Technical Paper Series. http://dx.doi.org/10.4271/2007-01-1236.

Davidson, Lars, 2009. Large eddy simulations: How to evaluate resolution. Int. J. Heat Fluid Flow 30 (5), 1016–1025. http://dx.doi.org/10.1016/j.ijheatfluidflow.2009.06.006.

Ekman, Petter, Larsson, Torbjörn, Virdung, Torbjörn, Karlsson, Matts, 2019. Accuracy and speed for scale-resolving simulations of the drivaer reference model. In: SAE Technical Paper Series. http://dx.doi.org/10.4271/2019-01-0639.

Ekman, Petter, Venning, James, Virdung, Torbjörn, Karlsson, Matts, 2021. Importance of sub-grid scale modeling for accurate aerodynamic simulations. J. Fluids Eng. 143 (1), http://dx.doi.org/10.1115/1.4048351.

Germano, Massimo, Piomelli, Ugo, Moin, Parviz, Cabot, William H., 1991. A dynamic subgrid-scale eddy viscosity model. Phys. Fluids A 3 (7), 1760–1765. http://dx.doi.org/10.1063/1.857955.

Grandemange, M., Cadot, O., Courbois, A., Herbert, V., Ricot, D., Ruiz, T., Vigneron, R., 2015. A study of wake effects on the drag of Ahmed's squareback model at the industrial scale. J. Wind Eng. Ind. Aerodyn. 145, 282–291. http://dx.doi.org/10.1016/j.jweia.2015.03.004.

Grandemange, M., Gohlke, M., Cadot, O., 2013. Bi-stability in the turbulent wake past parallelepiped bodies with various aspect ratios and wall effects. Phys. Fluids 25 (9), http://dx.doi.org/10.1063/1.4820372.

He, Kan, Minelli, Guglielmo, Su, Xinchao, Gao, Guangjun, Krajnović, Siniša, 2022. On state instability of the bi-stable flow past a notchback bluff body. J. Fluid Mech. 931, http://dx.doi.org/10.1017/jfm.2021.1025.

Howell, Jeff, Le Good, Geoff, 1999. The influence of aerodynamic lift on high speed stability. SAE Tech. Paper Ser. Tech. 01 (0651), 8. http://dx.doi.org/10.4271/1999-01-0651.

Jessing, Christoph, Wilhelmi, Henning, Wittmeier, Felix, Wagner, Andreas, Wiedemann, Jochen, Dillmann, Andreas, 2020. Investigation of transient aerodynamic effects on public roads in comparison to individual driving situations on a test site. In: SAE Technical Paper Series. http://dx.doi.org/10.4271/2020-01-0670.

Josefsson, Erik, 2022. Tyre Aerodynamics of Passenger Vehicles (Licentiate thesis). Chalmers University of Technology.

Josefsson, Erik, Hobeika, Teddy, Sebben, Simone, 2022. Evaluation of wind tunnel interference on numerical prediction of wheel aerodynamics. J. Wind Eng. Ind. Aerodyn. 224, http://dx.doi.org/10.1016/j.jweia.2022.104945.

Kawakami, Mitsuyoshi, Murata, Osamu, Maeda, Kazuhiro, 2015. Improvement in vehicle motion performance by suppression of aerodynamic load fluctuations. SAE Int. J. Passeng. Cars - Mech. Syst. 8 (1), 205–216. http://dx.doi.org/10.4271/2015-01-1537.

Lawson, Andrew A., Sims-Williams, David B., Dominy, Robert G., 2008. Effects of on-road turbulence on vehicle surface pressures in the A-pillar region. SAE Int. J. Passeng. Cars - Mech. Syst. 1 (1), 333–340. http://dx.doi.org/10.4271/2008-01-0474.

Ljungskog, Emil, 2019. Evaluation and Modeling of the Flow in a Slotted Wall Wind Tunnel (Ph.D. thesis). Chalmers University of Technology.

Ljungskog, Emil, Sebben, Simone, Broniewicz, Alexander, 2020. Inclusion of the physical wind tunnel in vehicle CFD simulations for improved prediction quality. J. Wind Eng. Ind. Aerodyn. 197, http://dx.doi.org/10.1016/j.jweia.2019.104055.

Matsumoto, Daiki, Nakae, Yusuke, Niedermeier, Christoph, Tanaka, Hiroshi, Indinger, Thomas, 2019. Application of dynamic mode decomposition to influence the driving stability of road vehicles. In: SAE Technical Paper Series. http://dx.doi.org/10.4271/2019-01-0653.

Meile, W., Ladinek, T., Brenn, G., Reppenhagen, A., Fuchs, A., 2016. Non-symmetric bi-stable flow around the Ahmed body. Int. J. Heat Fluid Flow 57, 34–47. http://dx.doi.org/10.1016/j.ijheatfluidflow.2015.11.002.

Menter, F., 2018. Stress-blended eddy simulation (SBES)—A new paradigm in hybrid RANS-LES modeling. In: Progress in Hybrid RANS-LES Modelling. In: Notes on Numerical Fluid Mechanics and Multidisciplinary Design, Springer International Publishing, ISBN: 978-3-319-70031-1, pp. 27–37. http://dx.doi.org/10.1007/978-3-319-70031-1_3, book section Chapter 3.

Milliken, William F., Dell'Amico, Fred, Rice, Roy S., 1976. The static directional stability and control of the automobile. In: SAE Technical Paper Series. http://dx.doi.org/10.4271/760712.

Okada, Yoshihiro, Nouzawa, Takahide, Nakamura, Takaki, Okamoto, Satoshi, 2009. Flow structures above the trunk deck of sedan-type vehicles and their influence on high-speed vehicle stability 1st report: on-road and wind-tunnel studies on unsteady flow characteristics that stabilize vehicle behavior. SAE Int. J. Passeng. Cars - Mech. Syst. 2 (1), 138–156. http://dx.doi.org/10.4271/2009-01-0004.

Perry, Anna-Kristina, Pavia, Giancarlo, Passmore, Martin, 2016. Influence of short rear end tapers on the wake of a simplified square-back vehicle: wake topology and rear drag. Exp. Fluids 57 (11), http://dx.doi.org/10.1007/s00348-016-2260-3.

Schuetz, Thomas, 2015. Aerodynamics of Road Vehicles, fifth ed. ISBN: 978-0-7680-7977-7, http://dx.doi.org/10.4271/r-430.

Theissen, Pascal, 2012. Unsteady Vehicle Aerodynamics in Gusty Crosswind (Ph.D. thesis). Technical University of Munich.

Törnell, Johannes, Sebben, Simone, Söderblom, David, 2021. Influence of inter-vehicle distance on the aerodynamics of a two-truck platoon. Int. J. Automot. Technol. 22 (3), 747–760. http://dx.doi.org/10.1007/s12239-021-0068-5.

Urquhart, Magnus, Sebben, Simone, Sterken, Lennert, 2018. Numerical analysis of a vehicle wake with tapered rear extensions under yaw conditions. J. Wind Eng. Ind. Aerodyn. 179, 308–318. http://dx.doi.org/10.1016/j.jweia.2018.06.001.

Urquhart, Magnus, Varney, Max, Sebben, Simone, Passmore, Martin, 2020. Aerodynamic drag improvements on a square-back vehicle at yaw using a tapered cavity and asymmetric flaps. Int. J. Heat Fluid Flow 86, http://dx.doi.org/10.1016/j.ijheatfluidflow.2020.108737.

Watkins, Simon, Cooper, Kevin R., 2007. The unsteady wind environment of road vehicles, part two: Effects on vehicle development and simulation of turbulence. In: SAE Technical Paper Series. http://dx.doi.org/10.4271/2007-01-1237.

Wickern, Gerhard, Beese, Eckard, 2002. Computational and experimental evaluation of a pad correction for a wind tunnel balance equipped for rotating wheels. In: SAE Technical Paper Series. http://dx.doi.org/10.4271/2002-01-0532.

Windsor, Steve, Le Good, Geoff, 1993. The influence of aerodynamic lift on high speed stability. In: Autotech 93, Vol. 01. p. 8.

Wojciak, J., 2012. Quantitative Analysis of Vehicle Aerodynamics during Crosswind Gusts (Ph.D. thesis). Technical University of Munich.

Wordley, Scott, Saunders, Jeffrey W., 2008. On-road turbulence. SAE Int. J. Passeng. Cars – Mech. Syst. 1 (1), 341–360. http://dx.doi.org/10.4271/2008-01-0475.

Wordley, Scott, Saunders, Jeffrey W., 2009. On-road turbulence: Part 2. SAE Int. J. Passeng. Cars - Mech. Syst. 2 (1), 111–137. http://dx.doi.org/10.4271/2009-01-0002.